J Mater Sci (2008) 43:7465–7473
DOI 10.1007/s10853-008-2635-9

ULTRAFINE-GRAINED MATERIALS

Texture development in two-pass ECAE-processed beryllium

I. J. Beyerlein · R. D. Field · K. T. Hartwig · C. T. Necker

Received: 4 March 2008 / Accepted: 4 April 2008 / Published online: 13 July 2008

Abstract Texture development and substructure evolution are described for pure beryllium given two-pass equal channel angular extrusion (ECAE) processing following routes A and C. These routes impose different strain paths between the first and second passes—the former cross-shearing and the latter reversal. Polycrystal calculations that are in good agreement with the texture measurements suggest that basal slip and, secondly, prismatic slip are operative in both passes of both routes. Multi scale polycrystal modeling is shown to effectively predict texture evolution to strains of two caused by both ECAE processing routes. Shear-like deformation textures observed in the second pass of route C are explained by differences in deformation characteristics between the first and second passes.

Introduction

Equal channel angular extrusion (ECAE) is a well-known severe plastic deformation (SPD) process for reducing grain sizes down to the submicron (ultra-fine grain) or nano-scale (nano-crystalline) [1–3] in conventional metals. It also results in substantial texture development, that is, changes in the distribution of crystallographic orientations of the grains [4]. A single pass through an ECAE die imposes severe plastic deformation via simple shearing, with equivalent strains ranging from 0.8 to 1.1 for most ECAE tooling geometries. In this operation, the cross section of the workpiece (billet or bar) remains constant enabling re-insertion of the extruded bar into the die. Each new pass introduces a strain path change, and any rotation about the sample long axis prior to re-insertion alters the path change or so called "route." The first pass leads to significant texture changes, producing a typical simple shear texture which can be formally characterized by ideal simple shear components [5]. In multi-pass ECAE, the resulting cumulative severe plastic deformation through frequent strain path changes causes texture development in all crystal types to vary with processing route and number of passes. Texture development in such severely deformed samples is relevant because it contributes critically to anisotropy in elastic, plastic [6, 7], fracture, fatigue, creep, and superplastic behavior [8].

Influences of processing parameters, including pass number, die angle, and route, on texture development have been examined mainly in cubic metals, usually at room temperature (see [4] and references therein). There are far less ECAE texture studies on ECAE-processed hexagonal close packed (hcp) metals. Experimental work has been done on Ti, Be, Zr, and Mg and their alloys [9–16] processed at various temperatures. Theoretical studies have been limited to predicting texture development after one pass [14, 17–19], with the exception of [20], where the second pass of route A in Mg was also simulated. Compared to cubic metals, hcp metals present difficult challenges in characterization and modeling due to the

I. J. Beyerlein (✉)
Theoretical Division, Los Alamos National Laboratory, Los Alamos, NM, USA
e-mail: irene@lanl.gov

R. D. Field · C. T. Necker
Materials Science and Technology Division, Los Alamos National Laboratory, Los Alamos, NM, USA

K. T. Hartwig
Mechanical Engineering Department, Texas A&M University, College Station, TX, USA

multiplicity of deformation modes by slip and twinning. The combination of modes operating depends largely on the metal's c/a ratio (ratio of the long to short dimension of the unit cell) and individual grain orientation and secondly on processing temperature and strain rate, grain size, and alloying. The wide use of this class of metals and the strong dependency of their mechanical behavior on texture encourage more texture and anisotropy studies. In these, texture prediction should be an important component as this capability is critical for texture-property control and efficient forming operation design.

In this work we have examined texture development through measurement and multi-scale modeling in beryllium (Be) processed by ECAE routes A and C at 425 °C. These two routes impose different strains in going from the first to the second pass [2, 21]. Route A induces cross-shearing. For route C, the direction of shearing is reversed in the second pass. Beryllium has an hcp crystal structure and deforms primarily by basal slip [22–24]. Non-basal slip systems, such as prismatic and pyramidal <c+a>, and deformation twinning, are possible secondary modes. At 425 °C, Be is ductile and its deformation response exhibits the conventional work hardening stages II, III, and IV, characteristic of thermally activated slip (and no twinning) [25].

The key objective of our work is to extend modeling capabilities for texture development in hcp metals under SPD with a strain path change, including perhaps the most difficult one, a strain path reversal. Although the present work focuses on ECAE, many forming operations involve similar large strains and frequent strain path changes. Like Be, many other hcp metals, such as Zn, Cd, and Mg, also deform primarily by basal slip [23, 24].

ECAE extrusion and experimental techniques

For the current investigation, Be rods canned in Ni were subjected to both single- and two-pass ECAE processing. The starting material was powder metallurgy source Be (0.72 wt% BeO), designated as P31664, manufactured by the Brush-Wellman Company by vacuum hot pressing of attrited powder. Cylinders 0.75″ in diameter and 5.5″ long (19.1 mm × 139.7 mm) were extracted from the bulk using wire electro-discharge machining and then machined to fit into 1″ square by ∼5″ long (25.4 mm × 127 mm) Ni-200 cans with a central 0.75″ diameter hole bored for the Be cylinders. Before being placed in the cans the Be samples were vacuum-annealed for 1 h at 800 °C to relieve machining stresses. A plug with a step joint was then electron-beam-welded onto the top of the can.

Three billets were extruded: a single pass, two passes with no rotation (route A), and two passes with a 180° rotation (route C) about the sample long axis between passes. The extrusions were performed in a warm tool (350 °C) through a sharp 90° angle at a nominal billet temperature of 425 °C and with a punch velocity of 25.4 mm/s. An estimated upper limit for the corresponding strain rate is $\sim 10\ s^{-1}$, assuming the width of the shear zone is 10% of the billet thickness. For all extrusions a solid state lubricant was used. The peak loads seen for the first and second passes were nominally 250,000 and 350,000 lbs. force (1.11×10^6 and 1.56×10^6 N), respectively.

Thermodynamics considerations of the combined effects of rapid deformation, thermal isolation of the Be by the Ni can, and a lower temperature tool lead to an estimated Be temperature rise of ∼50 °C during extrusion and maximum adiabatic temperature of 490 °C [26]. Such temperature rises have been measured and calculated elsewhere [26–28]. A post-heat treatment study indicates that this temperature rise would not lead to recrystallization and grain growth. In this study, some pressed pieces were subjected to 1 h heat treatments at 600, 700, and 800 °C. No appreciable grain coarsening occurred below 800 °C. At 800 °C, the grain size approached that of the as-received material. Vickers hardness measurements showed decreasing strength for heat treatments at 600 °C and above, with the hardness returning to approximately that of the as-received material after the 800 °C treatment.

Microstructural characterization was performed using both optical and TEM techniques to investigate grain refinement and deformation microstructures. Metallographic preparation was standard. TEM foils were made by first taking 350–500 μm slices using a diamond saw in the flow (billet side) plane. The slices were then ground to ∼150 μm using 400–600 grit SiC paper and 3 mm discs removed using an abrasive core drill. The foils were thinned to perforation in a Fischione automatic electropolishing unit, using a solution of 8% perchloric acid, 20% water, 12% isobutyl alcohol, and 60% methanol at a temperature of −50 °C, and a potential of 65 V. TEM was performed in a Philips CM30 instrument at an accelerating potential of 300 KV.

Texture development was characterized by bulk X-ray diffraction (XRD). Raw texture intensities were collected on metallographic samples using a Scintag 5-axis X1 pole figure goniometer at 40 kV/20 mA, with a count time of 2 s and sample oscillation of 4 mm. Using the popLA software package [29], the (0001), $(10\bar{1}0)$, and $(10\bar{1}1)$ pole figures were corrected for background and defocusing and used to determine the orientation distribution function (ODF) with its WIMV algorithm. Full pole figures were re-calculated from the ODF.

Figure 1 shows optical and TEM micrographs of the as-received material. The grains are equi-axed with sizes ranging from 10 to 40 μm. TEM reveals tiny BeO particles in the grain boundaries. The initial texture was nearly random [17].

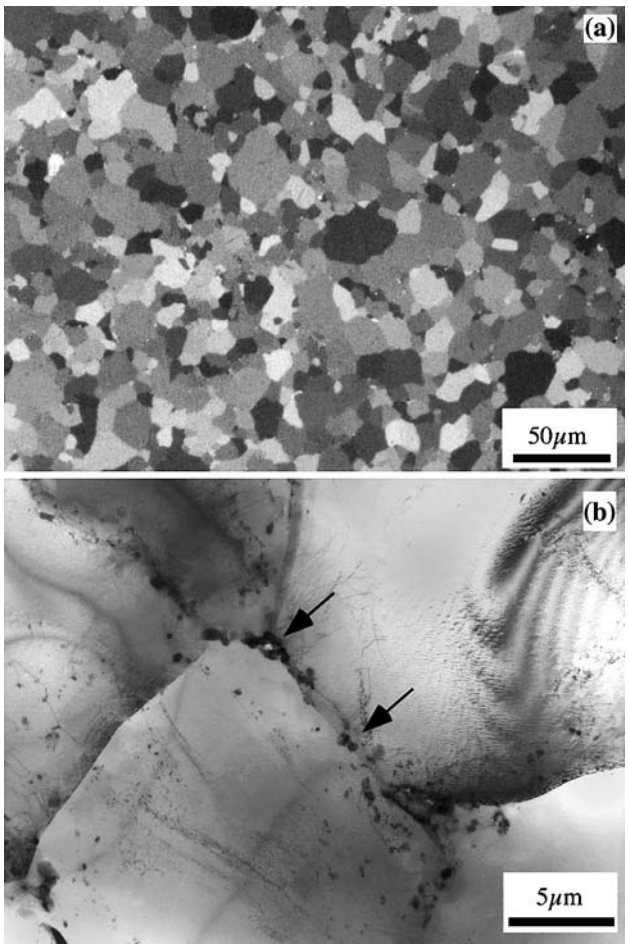

Fig. 1 Microstructures of the starting material prior to ECAE processing: (**a**) light optical micrograph and (**b**) TEM micrograph. The arrows in (**b**) indicate BeO particles

Experimental results

This section focuses on results for the two-pass material. A detailed examination of the one-pass material was presented previously [17]. For descriptions in the text below, the horizontal 1-axis is the extrusion axis (ED), the vertical 2-axis is parallel to the entry-channel axis (ND), and the 3-axis (FD) lies normal to the side plane of the ECAE die which we also call the flow plane.

Figure 2 shows cross sections of the two-pass billets in the flow plane. No cracking is observed in either billet. Figure 3 presents optical micrographs in the flow plane of the one-pass and two-pass materials. These images show that the grain shapes evolve as expected [2]. After one pass, the grains are elongated in nearly the same direction. After two-pass route A, the grains remain elongated and become more closely aligned with the extrusion direction. After two-pass route C, the grains are more or less equi-axed again. Continuum mechanics considerations predict that a sphere will deform into an ellipse with inclination 22.5 and 14.3°

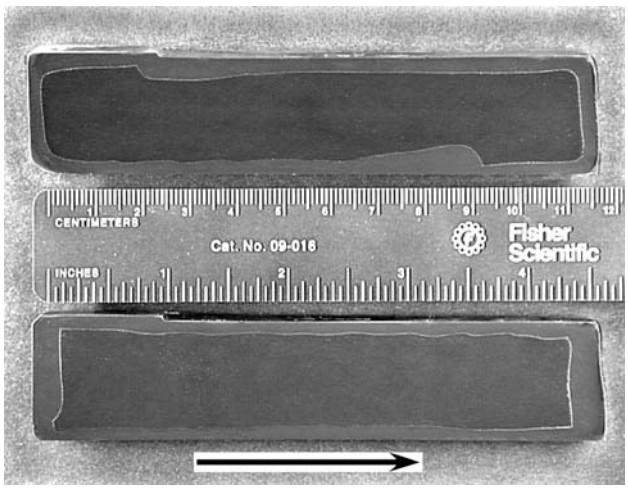

Fig. 2 Flow plane cross sections of the two-pass Ni canned Be billets. Top: route A. Bottom: route C. The arrow designates the extrusion direction

from the ED after one pass and two passes of route A, respectively, and will return to a sphere after two passes of route C [30]. Anisotropic polycrystal calculations predict inclinations of 20 and 15° after one- and two-pass route A, respectively [21]. Generally these predictions provide good estimates of the microstructural shape evolutions observed in Fig. 3. Optical microscopy of ingot source Be shows even more grain refinement after four passes of route Bc [12].

A curious feature seen in all the Fig. 3 micrographs is the appearance of localized microscopic bands. The nominal width and separation distance of these localizations are similar for all cases: 10 and 50 μm, respectively. This feature may help to explain the directional nature of the substructure seen at higher magnification (Fig. 4a). These are to be distinguished in length scale and origin from macroscopic shear bands, which have been associated with flow softening [31].

As shown in Fig. 4, low magnification TEM reveals that substructure development occurs in both routes, interestingly, with route A grains containing an elongated directional (bamboo-like) substructure, like in the first pass [17], while route C grains contain a more equi-axed cellular substructure. However, the route A specimen also contains fine subgrains, giving rise to further refinement of the microstructure and a more equi-axed appearance in higher magnification TEM (see Fig. 5). Twinning was not observed.

Texture developments after one pass and two passes of route A and C are compared in Fig. 6a using (0001) pole figures in the transverse plane. The transverse plane is parallel to the billet long axis direction. The first-pass texture exhibits a monoclinic symmetry and maximum intensity around 4.0 mrd (multiples of random distribution). The maximum (0001) pole densities are tilted roughly 25° from the ND-axis (2-axis). Despite the different strain path

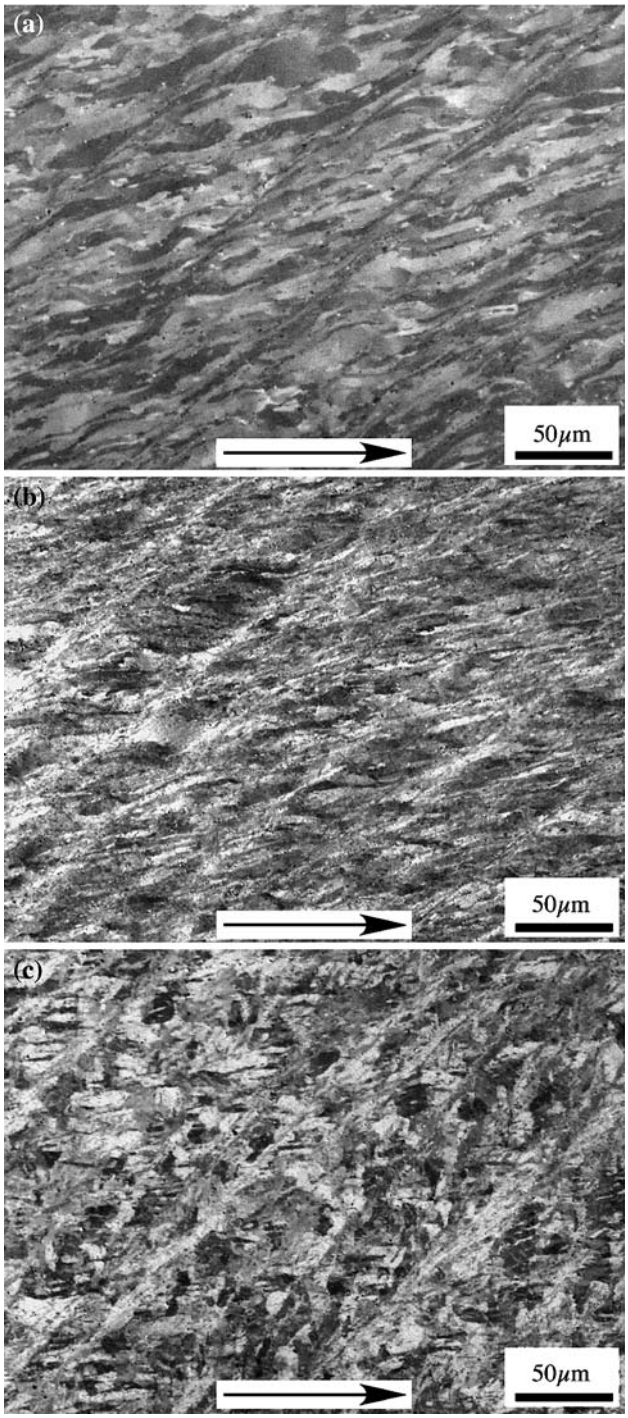

Fig. 3 Optical micrographs in the flow plane of the as-extruded (**a**) one-pass, (**b**) two-pass route A, and (**c**) route C material. The arrows show the extrusion direction

changes invoked by routes A and C, the second-pass textures have some features in common, namely a monoclinic symmetry and maximum intensities ranging from 3.5 to 4.0 mrd which are similar to that of the first pass. Also, in all cases, some very low intensity ($\sim$1 mrd) components are observed on the rim, near the ED. Differences are found in the location of the maxima: $\sim$15 and $\sim$35° from the ND-axis in route A and C, respectively. These maxima are more diffuse in the route C texture than those in the single-pass and two-pass route A textures.

Unlike in route A, the texture development observed in route C is not expected. Because the shearing direction is reversed in the second pass of route C, a return to the initial texture may be expected instead. Indeed this recovery is what standard polycrystal models would predict [21, 32].

The shear-like texture in the route C measurement, however, is similar to the unaltered shear textures observed after reverse torsion tests. These were first reported for iron, brass, and copper with much larger pre-strains [33] than in one ECAE pass. They have been observed more recently in [34, 35] with similar pre-strains but much weaker textures than observed here in the route C texture.

Our route C measurement is very similar to what has been reported in several previous ECAE texture studies on fcc and bcc metals [32, 36–44], and in those few studies on hcp metals [45, 46]. In these, shear-like textures after second, and higher even-numbered, passes of route C were observed albeit with varying intensities. The consistency of this result in fcc, bcc, and hcp metals alike suggests that the primary reason for unaltered shear textures following multi-pass route C processing must have little to do with the small-scale mechanisms that distinguish texture evolution in one material from another.

Next we briefly describe a multi-scale model used to understand and predict texture evolution during routes A and C. It will be suggested that the reason for shear-like route C textures is found in the largest length-scale component, the macroscopic ECAE deformation. The deformation in the second pass is not a pure reversal of the shear given in the first pass, which leads to a "residual" deformation shear texture after two passes of route C. This explanation should apply to nearly all metals, and is an important conclusion of this work.

Multi-scale method

Several 2D and 3D finite element studies have shown that for the same die geometry and lubrication, ECAE deformation characteristics depend on material behavior, e.g., [47, 48]. For sharp corner dies, like the one used here, when the material is strain hardening, a corner gap forms and a fan-like plastic deformation zone (PDZ) is generated [47, 49], as illustrated in Fig. 7a. When the material is perfectly plastic, however, it fills the die, and the deformation is close to simple shear [2, 47, 49] (Fig. 7b). Consequently, when the material strain hardens within the first 0.5 to 1.0 strain but not thereafter, the first-pass deformation would resemble Fig. 7a, and the second-pass

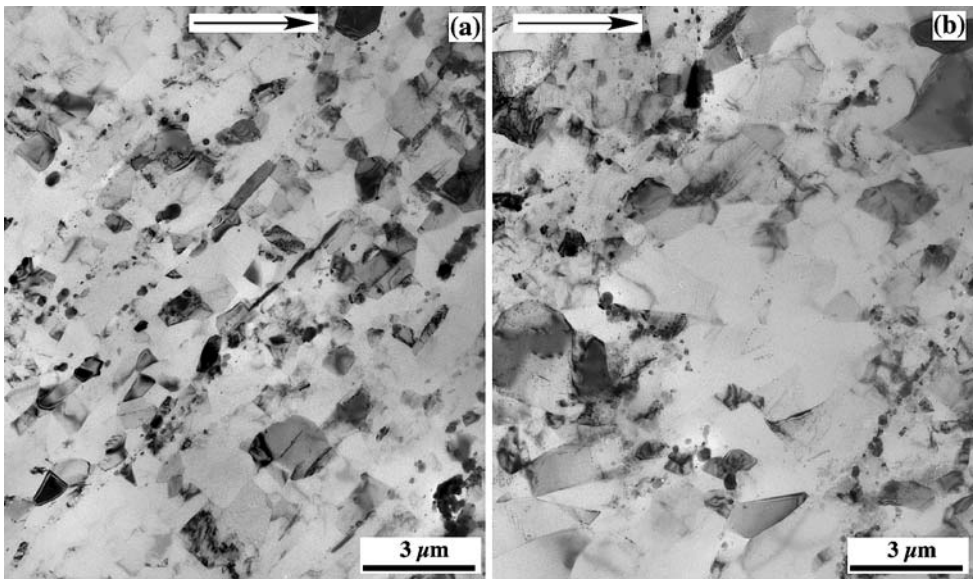

Fig. 4 Low magnification TEM micrographs in the flow plane of material: (**a**) as-extruded two-pass route A and (**b**) two-pass route C

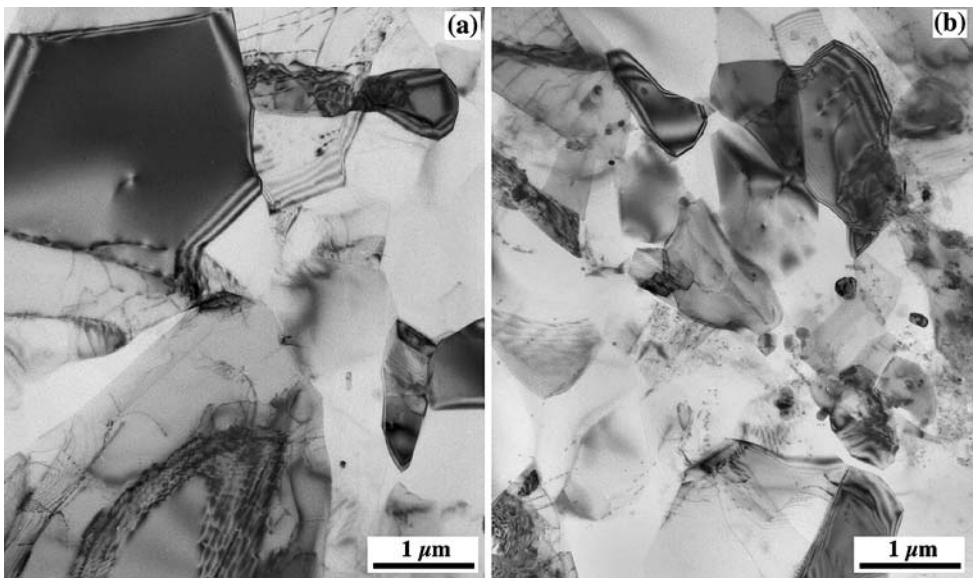

Fig. 5 High magnification TEM micrographs in the flow plane of the as-extruded two-pass (**a**) route A and (**b**) route C material

deformation, Fig. 7b. This or similar two-pass deformation pattern has been confirmed by FE simulations in [37, 50].

Hot-pressed Be is found to strain harden under compression at 425 °C ([25], private communication with D. W. Brown), a temperature which is sufficiently far below its recrystallization temperature. The deformation response exhibits stage II, stage III, and a weak stage IV, which are respectively dominated by dislocation storage, dynamic recovery, and possibly substructure evolution. The presence of well-developed substructures after two passes (Figs. 3–5) further supports the idea that dynamic recovery in the form of cross slip and climb occurred in Be at 425 °C. Therefore the deformation sequence in Fig. 7 should apply.

Rather than using FE simulations, we model the ECAE deformation described in Fig. 7 analytically. The velocity gradients used for each deformation are developed in [30] and found to agree well with FE simulations [51]. They are imposed uniformly and sequentially to a polycrystal, and the texture evolution is predicted by the visco-plastic self-consistent (VPSC) scheme [52]. The methodology for modeling the rotations corresponding to the ECAE routes is described in [21].

The development of VPSC was developed for low-symmetry metals like hcp Be, and explicitly incorporates anisotropic interactions between individual grains and the surrounding polycrystalline aggregate. Even for cubic crystal structures, the VPSC model proves to be superior to the Taylor model in predicting texture evolution during ECAE [32, 42, 43, 53]. The reasons have partly to do with large-strain deformation. Unlike the Taylor and Sachs models, self-consistent schemes allow for intergranular heterogeneities, which could grow with increased strain.

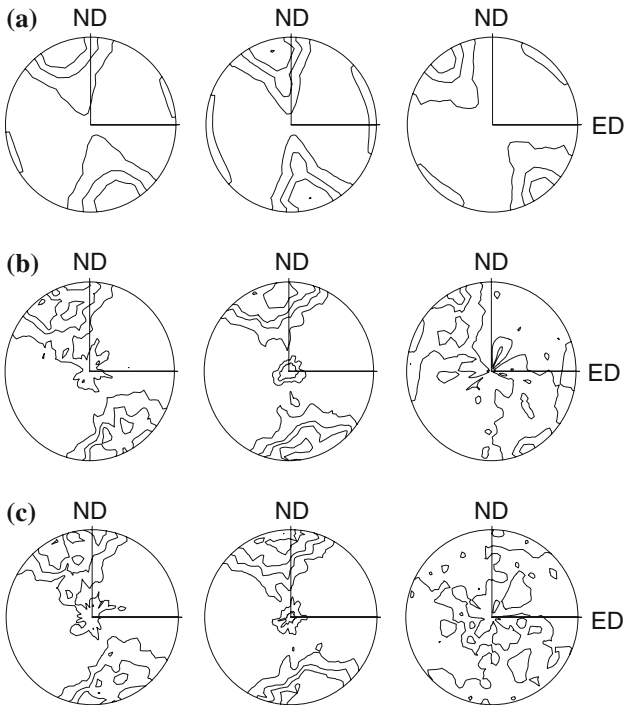

Fig. 6 (**a**) XRD measured basal pole figures of pure Be after a first pass, second pass route A, and second pass route C of ECAE processing with a sharp-corner $\Phi = 90°$ die. (**b**) Predicted texture evolution for the first two passes of routes A and C assuming the deformation sequence in Fig. 7 with PDZ $\beta = 10°$ in the first pass. (**c**) Predicted texture evolution assuming ideal uniform deformation in both passes (perfect reversal). Contour levels are 1/2/2.83/4.0 mrd

Like the actual starting material, VPSC simulations begin with a computer-generated random texture represented by 1,000 discrete orientations and initially spherical grains. A modified secant approximation is used. In this work, grain-grain interactions are simulated by invoking a co-rotation scheme [54], which slows down texture evolution and leads to intensities in better agreement with measurement [32, 55]. Also, in this and previous applications to ECAE, the shape of each grain is made to evolve according to its individual anisotropic response.

In the VPSC calculation, the hardening behavior of the critical resolved shear stresses τ_V in each Be grain follows an extended Voce law [56] and evolves differently according to its crystallographic orientation and strain history. Three slip modes are made available to each grain: basal slip, prismatic, and pyramidal <c+a>. Twinning was suppressed in this calculation because it was not experimentally observed. In the Voce law, τ_V for each of the basal, prismatic, or pyramidal <c+a> slip systems evolves with the total accumulated strain in the grain Γ according to

$$\tau_V(\Gamma) = \tau_0 + \left(\tau_1 + \theta_1^s \Gamma\right)[1 - \exp(-\theta_0 \Gamma/\tau_1)], \quad (1)$$

where the set of parameters (τ_0, τ_1, θ_0, and θ_1) are the same for each slip system belonging to the same slip mode. This phenomenological law models work hardening from stage II to stage IV. A different set, however, is estimated for each slip mode by fitting to mechanical test data of pure Be under monotonic loading at 425 °C ([25], Private communication D. W. Brown). The parameters corresponding to the fit are shown in Table 1. No attempt was made to adjust these parameters after either pass and the simulated ECAE textures that follow are fully predictive. We also have the option to assign latent hardening parameters between these modes, as was done for Zr [18] following Hill [57], but due to lack of experimental evidence, we set all latent hardening parameters to unity.

The macroscale model (Fig. 7) works in series with the VPSC model and Eq. 1. Of course, a fully coupled finite-element/polycrystal/crystal plasticity/single-crystal hardening formulation would prove more accurate, but no more effective in demonstrating our point that shear textures after two passes of route C result from differences in the macroscale deformation between the first and second passes.

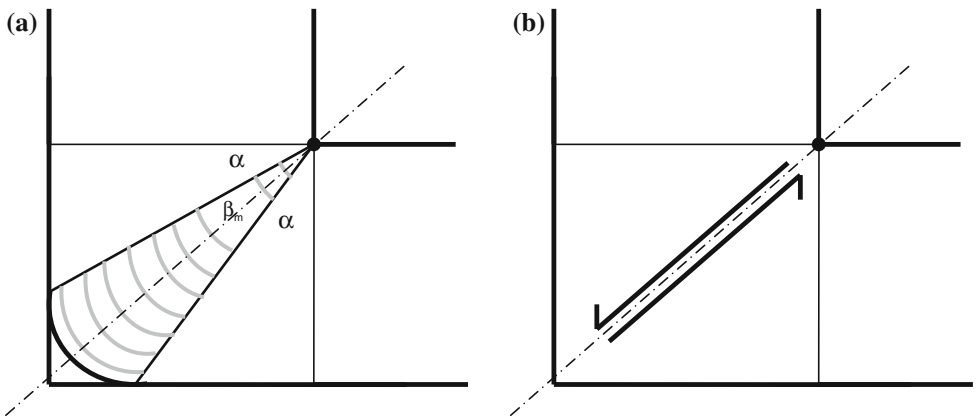

Fig. 7 Hypothetical sequence of deformation in two passes of ECAE for a die with a sharp outer corner angle. (**a**) First pass deformation characteristics. The deformation spreads out over a fan-shaped zone and a corner gap forms due to strain hardening. (**b**) Second pass deformation is close to ideal simple shearing because work hardening in the material has saturated. β_m is the fan angle; the angles on either side of the fan angle α are equal

Table 1 Deformation modes and Voce parameters associated with Eq. 1 for 99.9% Be at 425 °C. Latent hardening between all modes is 1.0

Deformation mode	τ_0 (MPa)	τ_1 (MPa)	θ_0 (MPa)	θ_1 (MPa)
Basal slip	100	130	3,500	0
Prismatic slip	150	150	4,500	70
Pyramidal <c+a> slip	420	1,100	1E + 05	0

Modeling interpretations and discussion

Figure 6b presents the simulated (0001) pole figures corresponding to the measured cases in Fig. 6a. The model captures the main features of each texture: the location of the maxima from the ND-axis, the intensities (4.3, 4.7, and 3.6 mrd for one-pass, two-pass A, and two-pass C, respectively), and the monoclinic symmetry. Most importantly, the two-pass route C texture contains relatively strong shear components, consistent with the measurement. Minor discrepancies are the low intensity components predicted near the FD and the lack of those at the rim near the ED.

For the predictions in Fig. 6, the model calculates the contribution of each slip mode averaged over all grains in the polycrystal. In the first pass, basal slip was the most active (~65%), followed by prismatic slip. Basal slip becomes more active in the second pass, ~70% for route A and 80% for route C. The increase in basal activity can be easily explained when considering texture development. The texture produced after the first pass and subsequent rotations for route C results in a second-pass 'entry texture' that favorably orients a majority of the grains for easy basal slip in the second pass. Pyramidal slip was negligible in any case. However, this slip mode was identified in TEM analysis of the single pass specimen and attributed to local accommodation at grain boundaries [17].

For comparison, Fig. 6c shows the texture predictions assuming ideal simple shearing for both ECAE extrusions, in which case the macroscopic strain path is a pure reversal. The same material model assuming grain-grain interactions, individual grain shape evolution, and anisotropic hardening was used. In this case, the route A texture is practically unaffected by the change. In route C, however, the initial texture is nearly recovered. The relative activities of basal, prismatic, and pyramidal do not change appreciably from those in Fig. 6b.

The modeling results show that the observed texture development in route C can be explained by a large difference in deformation characteristics between the first and second pass. The plausibility of this hypothesis was first demonstrated in Mahesh et al. [58] in copper ECAE-pressed using a rounded corner die. In this case, a fan-shaped deformation zone develops in every pass, but is skewed in the first pass relative to the second due to strain hardening in the first pass [43]. There are, of course, other possible factors that could explain shear-like textures in route C, such as grain-grain interactions, texture gradients across the ECAE sample [32], substructure development [58, 59], work hardening, and latent hardening [37]. All calculations in Fig. 6 accounted for grain–grain interactions in an approximate way using the co-rotation scheme; however, the calculation in Fig. 6c assuming a perfect reversal could not reproduce the second-pass route C measurement. Certainly texture measurements made over large regions of a sample containing significant texture gradients (particularly with shear textures in the surface layers) will lead to weak shear textures on average [32]. However, spatially resolved texture measurements in the central homogeneous region of a two-pass route C sample also produced shear textures [37]. Sophisticated theoretical models for substructure evolution, which involve development of intergranular regions misoriented from the parent grain, have been developed and applied to ECAE [58–60]. While implementing these subgrain models into either a Taylor [58], or VPSC [59] formulation predicted second-pass shear textures, they were still much weaker than the copper measurement. Previous work on copper [37] suggests that anisotropic hardening, simulated by affecting latent hardening, could lead to weak shear textures after a reversal. In the present case of hcp Be, the hardening was anisotropic, and yet, as shown in Fig. 6c for a perfect reversal, this alone did not lead to relatively strong shear textures in two-pass route C. Although not presented, we tested latent hardening parameters greater than unity for Be and this did not change the result appreciably from that shown in the perfect reversal calculation, Fig. 6c.

In summary, while each alternative explanation above is certainly plausible, none alone can explain the generation of a complete shear texture in the second pass of route C. We show here that the more effective explanation is given by changes in deformation characteristics, such as the fan-shaped plastic deformation zone in pass one changing to a more ideal simple shearing in going from pass one to pass two (see Fig. 7). When Fig. 7 is applied to route C (with the 180° twist) the sense of shearing in the second pass is still largely reversed from the first, but it is not a *perfect* reversal. The present model suggests that this slight imperfection can result in a shear deformation texture in even passes of route C. The microstructure, on the other hand, is not as sensitive to this minor deviation from a pure reversal. Both measurement and modeling find nearly equiaxed grain shapes after the second pass of route C. This is a reflection of the fact that, again, the sense of shearing is largely reversed, even when the sequence shown in Fig. 7 is applied to route C.

Conclusions

A multi-scale ECAE model is shown to effectively predict texture evolution in Be for two-pass route A and route C processing (see Fig. 6b). In principle, the sample experiences shearing on different planes in route A and on the same plane but in the reverse direction in route C. Both routes generate simple shear textures with monoclinic symmetry and strengths $\sim$4 mrd, much like after one pass. Model results suggest that the nearly unaltered shear texture in route C is due to differences in the macroscale deformation characteristics between the first and second pass. Anisotropic hardening, which is strong in Be, and grain-grain interactions cannot explain this result. Optical and TEM microscopy show that substructure evolution is substantial with no evidence of twinning. Substructure evolution, which is the usual explanation for unaltered shear textures after a strain reversal, was not included in our modeling. However, previous experimental and theoretical studies in cubic metals imply that with only $\sim$1.0 strain per pass, substructure development is not significant enough to impact texture evolution after a few passes, and second-pass route C textures would still be much weaker than observed here.

Acknowledgements The authors would like to thank Pallas Papin for her assistance in preparing and performing preliminary examinations of TEM foils, and Dr. Robert Hanrahan for technical discussions. Technical discussions with Dr. Dan Thoma and Steve Abeln also contributed significantly to this work. Work at LANL was supported by U.S. DOE Contract No. W-7405-ENG-36. IJB would also like to acknowledge support by a Los Alamos Laboratory Directed Research and Development Project (No. 20030216) and the Office of Basic Energy Sciences Project FWP 06SCPE401.

References

1. Segal VM (1974) Sc.D. Thesis, Minsk (in Russian)
2. Segal VM (1995) Mater Sci Eng A197:157. doi:10.1016/0921-5093(95)09705-8
3. Valiev RZ, Langdon TG (2006) Prog Mater Sci 51:881. doi:10.1016/j.pmatsci.2006.02.003
4. Beyerlein IJ, Toth LS (2008) In: Zehetbauer M, Zhu YT (eds) Bulk nanostructured materials. Wiley-VCH, Germany (in press)
5. Li S, Beyerlein IJ, Bourke MAM (2004) Mater Sci Eng A394:66
6. Yapici GG, Beyerlein IJ, Karaman I et al (2007) Acta Mater 55:4603. doi:10.1016/j.actamat.2007.03.031
7. Beyerlein IJ, Alexander DJ, Tomé CN (2007) J Mater Sci 42:1733. doi:10.1007/s10853-006-0906-x
8. Sakai G, Horita Z, Langdon TG (2004) Mater Trans 45:3079. doi:10.2320/matertrans.45.3079
9. Agnew SR, Mehrotra P, Lillo TM et al (2005) Mater Sci Eng 408A:72
10. Choi WS, Ryoo HS, Hwang SK et al (2002) Metall Mater Trans 33A:973
11. Yoshida Y, Cisar L, Kamado S (2003) Mater Sci Forum 419–422:533
12. Li S, Alexander DJ, Beyerlein IJ et al (2008) ICOTOM-15 (in press)
13. Kim WJ, Hong SI, Kim YS (2003) Acta Mater 51:3293. doi:10.1016/S1359-6454(03)00161-7
14. Yu SH, Chun YB, Hwang SK (2005) Phil Mag 85:345. doi:10.1080/14786430412331315752
15. Shin DH, Kim I, Kim J et al (2003) Acta Mater 51:983. doi:10.1016/S1359-6454(02)00501-3
16. Yu SH, Shin DH, Hwang SK (2004) In: Zhu YT et al (eds) Ultra fine-grain symposium III. TMS (The Minerals, Metals & Materials Society), Warrendale, Pennsylvania
17. Field RD, Hartwig KT, Necker CT et al (2002) Metall Mater Trans 33A:965
18. Yapici GG, Beyerlein IJ, Tome CN et al (2008) Acta Mater (in preparation)
19. Vogel SC, Alexander DJ, Beyerlein IJ et al (2003) Mater Sci Forum 426–432:2661
20. Agnew SR, Mehrotra P, Lillo TM et al (2005) Acta Mater 53:3135. doi:10.1016/j.actamat.2005.02.019
21. Beyerlein IJ, Lebensohn RA, Tomé CN (2003) Mater Sci Eng 345A:122
22. Aldinger F (1979) In: Webster D, London GJ (eds) Beryllium science and technology. Plenum Press, New York
23. Price PB (1963) In: Thomas G, Washburn J (eds) Electron microscopy and strength of crystals. Div. of John Wiley and Sons, New York
24. Yoo MH, Wei CT (1966) Phil Mag 14:573. doi:10.1080/14786436608211952
25. Brown DW, Agnew SR, Abeln SP et al (2005) Mater Sci Forum 495–497:1037
26. Semiatin SL, Berbon PB, Langdon TG (2001) Scripta Mater 44:135. doi:10.1016/S1359-6462(00)00565-0
27. Yamaguchi D, Horita Z, Nemoto M, Langdon TG (1999) Scripta Mater 41:791. doi:10.1016/S1359-6462(99)00233-X
28. Kim HS (2001) Mater Trans 42:536. doi:10.2320/matertrans.42.536
29. Kocks UF, Canova GR, Tomé CN et al (1988) Computer Code LACC-88-6. Los Alamos National Laboratory, Los Alamos
30. Beyerlein IJ, Tomé CN (2004) Mater Sci Eng A380:171. doi:10.1016/j.msea.2004.03.063
31. Segal VM (1999) Mater Sci Eng A271:322
32. Li S, Beyerlein IJ, Alexander DJ et al (2005) Acta Mater 53:2111
33. Backofen WA (1950) Trans AIME 188:1454
34. Rollett AD, Lowe TC, Kocks UF et al (1988) In: Proc. ICOTOM-8. Warrendale, PA, 473 pp
35. Anand L, Kalidindi SR (1994) Mech Mater 17:223. doi:10.1016/0167-6636(94)90062-0
36. Tidu A, Wagner F, Huang WH et al (2000) J Phys IV France 10:211. doi:10.1051/jp4:20001023
37. Li S, Beyerlein IJ, Necker CT (2006) Acta Mater 54:1397. doi:10.1016/j.actamat.2005.11.020
38. Perlovich Y, Isaenkova M, Fesenko V et al (2006) Mater Sci Forum (NanoSPD3 Japan) 503–504:853
39. McNelley TR, Swisher DL (2004) In: Zhu YT et al (eds) Ultra-fine grained materials III. TMS (The Minerals, Metals & Materials Society), Warrendale, Pennsylvania
40. Ferrasse S, Segal VM, Kalidindi SR et al (2004) Mater Sci Eng 368A:28
41. Gibbs MA, Hartwig KT, Cornwell LR et al (1998) Scripta Mater 39:1699. doi:10.1016/S1359-6462(98)00384-4
42. Li S, Gazder AA, Beyerlein IJ et al (2006) Acta Mater 54:1087. doi:10.1016/j.actamat.2005.10.042
43. Li S, Gazder AA, Beyerlein IJ et al (2007) Acta Mater 55:1017. doi:10.1016/j.actamat.2006.09.022
44. Messemaeker JD, Verlinden B, Humbeeck JV (2005) Acta Mater 53:4245. doi:10.1016/j.actamat.2005.05.024
45. Isaenkova M, Perlovich Y, Fesenko V et al (2005) Mater Sci Forum 495–497:827

46. Perlovich Y, Isaenkova M, Fesenko V et al (2006) Mater Sci Forum (NanoSPD3 Japan) 503–504:859
47. Li S, Bourke MAM, Beyerlein IJ et al (2004) Mater Sci Eng A382:217
48. Zhernakov VS, Budilov IN, Kusimov ST et al (2007) Int J Mater Res 98:178
49. Kim HS, Seo MH, Hong SI (2000) Mater Sci Eng A291:86
50. Kim HS (2002) Mater Sci Eng A328:317
51. Li S, Beyerlein IJ, Alexander DJ (2005) Scripta Mater 52:1099. doi:10.1016/j.scriptamat.2005.02.008
52. Lebensohn RA, Tomé CN (1993) Acta Metall 41:2611. doi:10.1016/0956-7151(93)90130-K
53. Agnew SR, Kocks UF, Hartwig KT et al (1998) In: Proceedings of the 19th Risø International Symposium on Materials Science. Risø National Laboratory, 201 pp
54. Tomé CN, Lebensohn RA, Necker CT (2002) Metall Mater Trans 33A:2635
55. Vogel SC, Beyerlein IJ, Bourke MAM (2002) Mater Sci Forum 408–412:673
56. Tomé CN, Canova GR, Kocks UF et al (1984) Acta Metall 32:1637. doi:10.1016/0001-6160(84)90222-0
57. Hill R (1966) J Mech Phys Solids 14:95. doi:10.1016/0022-5096(66)90040-8
58. Mahesh S, Beyerlein IJ, Tomé CN (2005) Scripta Mater 53:965. doi:10.1016/j.scriptamat.2005.06.017
59. Enikeev NA, Abdullin MF, Nazarov AA et al (2007) Int J Mater Res 98:167
60. Sivakumar SM, Ortiz M (2004) Comput Methods App Mech Eng 193:5177. doi:10.1016/j.cma.2004.01.036